

Surface Acoustic Cavitation Understood via Nanosecond Electrochemistry. 2. The Motion of Acoustic Bubbles

Emmanuel Maisonhaute,[†] Benjamin A. Brookes, and Richard G. Compton*

Physical & Theoretical Chemistry Laboratory, Oxford University, South Parks Road, Oxford OX1 3QZ, U.K.

Received: September 10, 2001; In Final Form: January 14, 2002

Acoustic cavitation considerably enhances the mass transport toward a surface. When suitably fast electrochemical equipment is used, periodic peak currents can be observed. Previous observations attributed these peaks to diffusion inside a thin liquid layer present between the electrode and the bubble (Maisonhaute, E.; White, P.C; Compton, R. G. *J. Phys. Chem. B* 2001, 105, 12087–12091). This paper provides a semiquantitative model for explaining the bubble behavior, leading to an estimation of the diffusion layer thickness as well as the time during which the bubble “discovers” the electrode. Layer thicknesses ranging from 25 nm for very high acoustic pressures up to ca. 60 nm for smaller ones are found. Collapse velocities are estimated to be more than hundreds meters per second. Moreover, between two collapses, a slow bubble movement apart from the surface is evidenced. The force balance responsible for the collapse is reexamined and the viscosity constraint found to be an important parameter in explaining the global behavior.

1. Introduction

Acoustic cavitation is a field of increasing interest.^{1,2} In solution the very high temperatures reached during bubble collapse lead to sonoluminescence³ and open up new synthetic methods and chemical transformations,^{4,5} whereas interaction of bubbles with surfaces allows ultrasonic cleaning^{6,7} and increased mass transport.⁸ However, fundamental investigations of bubble interactions with a surface are difficult because they need a method selectively sensitive to events occurring at the surface yet fast enough to follow the rapid bubble movements. An excellent picture of an acoustic bubble oscillating on a surface was obtained by Crum using photographic detection.⁹ However, the driving frequency was only 60 Hz. Standard conditions useful for ultrasound applications in biology,¹⁰ chemistry, and physics use kHz or MHz frequencies, and therefore differ very significantly. Because higher frequencies are used, the calculated equilibrium radius in solution is smaller (150 μm for a 20 kHz sound field¹¹) and hence physical parameters such as surface tension may play a more important role. Moreover, the Rayleigh–Plesset¹² equation describing the bubble behavior is highly nonlinear, and its numerical solution is very sensitive to the experimental parameters. Furthermore, the internal bubble composition may also vary with the technique used to create the cavity, the solution composition (concentration of dissolved gas, presence of cavitation nuclei, etc.) and of course the presence of a boundary. As a consequence, to our knowledge, little data are available to describe the cavitation activity close to a surface in the kHz range.

In a recent paper,¹³ we reported chronoamperometry and cyclic voltammetry experiments performed using microelectrodes and fast electrochemical apparatus.^{14,15} The interpretation of the periodic chronoamperometric currents obtained for the one

electron reduction of $\text{Fe}(\text{CN})_6^{3-}$ under 20 kHz ultrasound led us to describe the bubble behavior as follows. For most of the time, the bubble size is a maximum. The bubble then blocks the electrode, leading to a negligible current. Subsequently, a very fast collapse occurs, and a new fresh solution is brought to the electrode surface. A rapid increase of the current is then observed. The bubble then returns to its maximum size, blocking the electrode again and the current drops. Different oscillating frequencies were observed, corresponding to harmonics or subharmonics of the driving frequency (20 kHz). For example, Figure 1a shows the chronoamperometric trace obtained for the reduction of $\text{Ru}(\text{NH}_3)_6^{3+}$ (−0.8 V vs Pt) in aqueous solution. The bubble oscillates here at 20 kHz. Chronoamperometric measurements performed with array of electrodes revealed that the single bubble signals could extend simultaneously over various distances. This was interpreted in terms of the possibility of having bubbles of different diameters, ranging from less than 15 μm up to 0.8 mm. A direct photographic detection confirmed this analysis. Moreover, using cyclic voltammetry, a depletion in the voltammetric peak was observed, proving that the distance between the electrode and the bubble was smaller than the created diffusion layer (ca. 100 nm). A similar depletion was observed simultaneously for another electrode separated from the first one by ca. 200 μm , which suggested that the bubbles were hemispherical rather than spherical.

It was therefore deduced that contrary to previous inferences albeit based on data pertaining to much lower frequencies, the peak currents were not due to a liquid microjet of solution propelled inside the bubble.^{16–18}

This paper presents a simple model of bubble implosion close to a surface, integrating the distance x_0 between the bubble and the surface as well as the collapse velocity v . A comparison with the experimental data obtained under different conditions then allows us to determine the key parameters that influence the peak currents. This analysis is then a first approach in the quantification of the bubble behavior.

* To whom correspondence should be addressed. Telephone: UK (0) 1865 277 432. Fax: UK (0) 1865 277 010. E-mail: Richard.Compton@chemistry.ox.ac.uk.

[†] Present address: Departement de Chimie, Ecole Normale Supérieure, UMR CNRS 8640, 24 rue Lhomond, 75231 Paris Cedex 05, France.

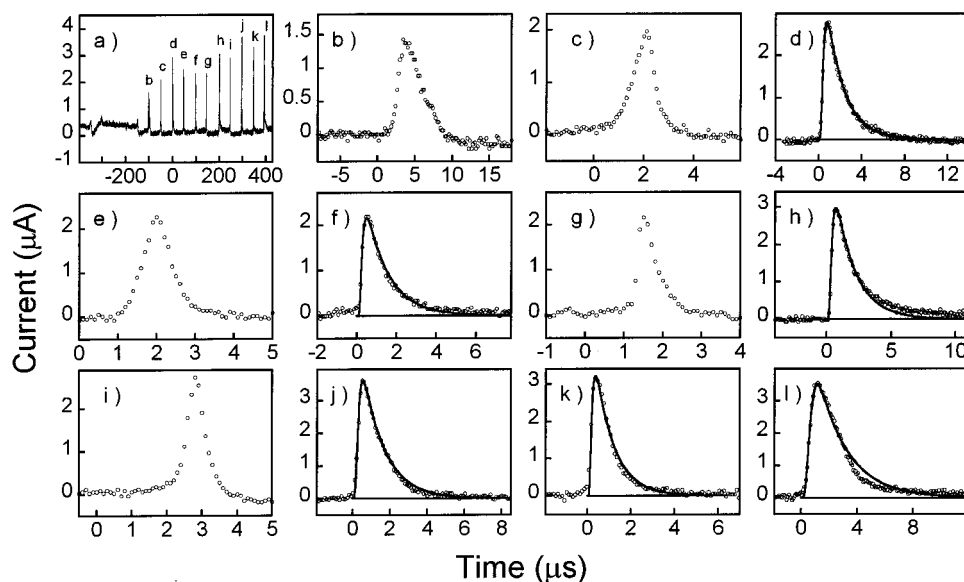


Figure 1. (a) Single bubble cavitation chronoamperometric current recorded for a 10 mM $\text{Ru}(\text{NH}_3)_6\text{Cl}_3$ + 0.1 M KNO_3 water solution under sonication at 20 kHz with a 13 mm conical horn, when the electrode potential is held at -0.8 V vs Pt, corresponding to the one electron reduction of $\text{Ru}(\text{NH}_3)_6^{3+}$. Electrode to horn distance: 7 mm. Acoustic power: 8.9 W cm^{-2} . Electrode diameter: $32 \mu\text{m}$. (b–l): Experimental spikes labeled in Figure 1a (circles) and simulated spikes (solid line) using the theory developed in section 3.1 where possible. Parameters of the simulations are given in Table 1.

2. Experimental Section

Reagents. Chemical reagents were used as follows: $\text{Ru}(\text{NH}_3)_6\text{Cl}_3$, $\text{K}_3\text{Fe}(\text{CN})_6$, and KNO_3 (Aldrich) were used as received. Argon bubbling (Pureshield, BOC) was used to maintain an inert atmosphere. Aqueous solutions were prepared using UHQ grade water of resistivity of not less than $18 \text{ M}\Omega \text{ cm}$ (Elga, High Wycombe, Bucks, U.K.).

Potentiostat. The rise time of the chronoamperometric signals for cavitation activity in aqueous solution could be as small as 200 ns, so very fast equipment is needed. We used a fast potentiostat generously provided by Amatore and described previously, which is able to allow scan rates as high as $2.5 \times 10^6 \text{ V s}^{-1}$ in cyclic voltammetry with full ohmic drop compensation.^{14,15} It was used here with a gain of $3.3 \times 10^4 \Omega$, and minimum filtering. The rise time measured on a pure capacitance in those conditions was 100 ns. No ohmic drop compensation was required for the chronoamperometric currents reported below since the applied potential was at least 0.5 V more negative than the standard potential of the electroactive species. The potential was applied with a TTI TG1304 programmable function generator (Thandar), and the current were recorded with a Tektronix TDS3032 oscilloscope.

Microelectrodes. Single microelectrodes of diameters of 32 and $139 \mu\text{m}$ were made by sealing platinum wires into soft glass.¹⁹

Ultrasonic Equipment. A 1.3 mm diameter titanium ultrasound horn transducer system (Sonics & Materials, VCX400) was used. The horn was conical or flat, and calibrated according to a published procedure.^{5,20}

Simulations. The Fick equation of diffusion for $t \geq t_0$ was solved numerically by fully explicit finite difference using Matlab 5. The flux was estimated by a second-order approximation. Using 50 space points resulted in 0.1% accuracy compared to a simulation run with 500 points.

3. Theory

We consider in this section the influence of the distance x_0 between the disk electrode and the bubble wall, with the aim

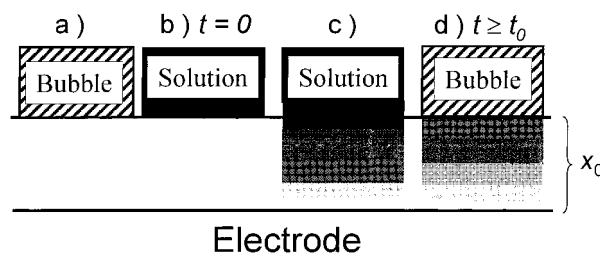


Figure 2. Description of the model. (a) $t \leq 0$, $C = 0$ inside TL. (b) $t = 0$, collapse ($C = 0$ inside TL, $C = C_0$ outside). (c) $0 \leq t \leq t_0$, diffusion from the bulk toward TL. (d) $t_0 \leq t$, the bubble wall returns. In Figure 2c,d, the gray scale features the concentration levels. Black: $C = C_0$. White: $C = 0$.

of describing chronoamperometric transient currents recorded at an electrode under transport limited conditions in the presence of cavitation. Therefore, considering a reduction, we suppose that the electrode is held at a potential negative enough so that the concentration C of electroactive compound at the electrode surface is zero. Therefore, diffusion of the electroactive material from the solution ($C = C_0$) toward the electrode ($C = 0$) occurs. A schematic of the model is given in Figure 2. For $t \leq 0$, the bubble grows and covers the electrode. The thin layer of thickness x_0 above the electrode (called TL in the following) is fully electrolyzed: the concentration of the electroactive species in TL and the current are then both zero (Figure 2a). When the collapse occurs (at $t = 0$, Figure 2b), bulk solution instantaneously replaces the bubble above TL and diffusion of the electroactive compound inside TL occurs (Figure 2c). We assume therefore that after the collapse there is no convection. We then neglect the macroscopic flow of solution produced by acoustic streaming,²¹ as it was shown before¹³ that it corresponds to a diffusion layer of size in the micrometer range, which is much larger than the diffusion layers involved in the experiments reported here (at most 100 nm, as will be seen in the following). After a time t_0 , we suppose that the bubble expands again, thus recreating another thin layer of same thickness x_0 . The electrode is then blocked again, and the current drops to zero within a time proportional to x_0^2/D (Figure 2d).

Two limiting situations are examined here. In section 3.1, the collapse velocity v is considered as infinite. This means that the time for the wall to “discover” the electrode $t_{\text{all}} \approx 2r_0/v$ (vide section 3.2) must be small compared to that needed for the electroactive material to reach the electrode surface by diffusion (ca. x_0^2/D), i.e., $v \gg 2r_0D/x_0^2$ must be fulfilled.

Conversely, in section 3.2, we suppose that $v \ll 2r_0D/x_0^2$ which allows us to consider the influence of v and of the geometry of the system.

3.1. Case 1: $v \gg 2r_0D/x_0^2$. Here the electrode is supposed to be discovered instantaneously, so the current density is the same over the whole electrode surface. The global current i is then proportional to the electrode area whatever the electrode geometry. It is also proportionnal to the flux of matter according to Fick's first law of diffusion:

$$i = nFAD \left(\frac{\partial C}{\partial x} \right)_{x=0} \quad (1)$$

where F , A , D , and x are respectively the Faraday constant, the electrode area, the diffusion coefficient, and the distance from the electrode.

The boundary conditions are then as follows:

$$t \leq 0, \quad x \leq x_0, \quad C = 0 \quad (2)$$

$$t = 0, \quad x \geq x_0, \quad C = C_0 \quad (3)$$

$$t \geq 0, \quad x = 0, \quad C = 0 \quad (4)$$

$$t \geq t_0, \quad x = x_0, \quad D \left(\frac{\partial C}{\partial x} \right)_{x=x_0} = 0 \quad (5)$$

Equation 5 means that there is no flux at $x = x_0$ when the bubble blocks the electrode.

3.1.1. Analytical Expression for $t \leq t_0$. The second Fick law to solve is

$$\frac{\partial C}{\partial t} = D \frac{\partial^2 C}{\partial x^2} \quad (6)$$

Equation 6 can be solved in the Laplace plane considering the boundary conditions, expressions 2–4. Returning to the real space allows us to get the concentrations and the current as function of t and x_0 :

$$x \leq x_0, \quad C = \left(\frac{C_0}{2} \right) \left(\operatorname{erfc} \left(\frac{x_0 - x}{2\sqrt{Dt}} \right) - \operatorname{erfc} \left(\frac{x_0 + x}{2\sqrt{Dt}} \right) \right) \quad (7)$$

$$x \geq x_0, \quad C = C_0 - \left(\frac{C_0}{2} \right) \left(\operatorname{erfc} \left(\frac{x - x_0}{2\sqrt{Dt}} \right) + \operatorname{erfc} \left(\frac{x + x_0}{2\sqrt{Dt}} \right) \right) \quad (8)$$

for the concentration and

$$i = nFAD \left(\frac{\partial C}{\partial x} \right)_{x=0} = nFAC_0 \sqrt{\frac{D}{\pi t}} \exp \left(-\frac{x_0^2}{4Dt} \right) \quad (9)$$

for the current. The peak current is $i_p = nFAC_0(D/x_0) \sqrt{2/\pi e}$ for $t_p = x_0^2/2D$. The shape of the current for different x_0 values is given in Figure 3a.

Moreover, the charge entering in TL during the time t_0 is

$$Q = \left(\frac{nFAC_0}{2} \right) \int_0^{x_0} \left(\operatorname{erfc} \left(\frac{x_0 - x}{2\sqrt{Dt_0}} \right) - \operatorname{erfc} \left(\frac{x_0 + x}{2\sqrt{Dt_0}} \right) \right) dx \quad (10)$$

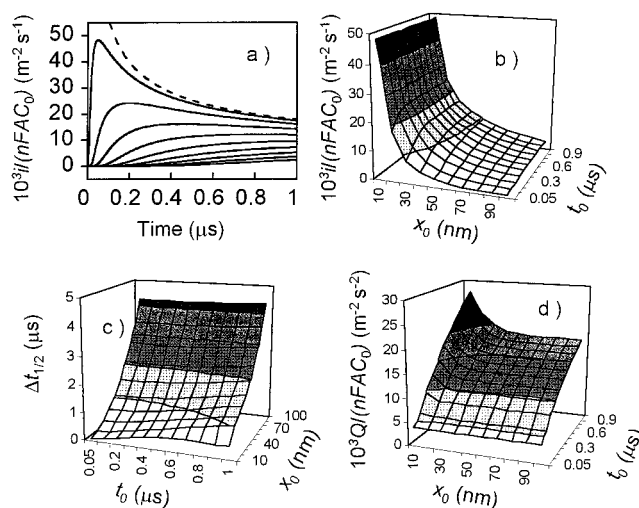


Figure 3. Figure 3a: Solid lines: analytical currents provided by case 1 for $t \leq t_0$, and $x_0 = 10, 20, 30, 40, 50, 60, 70, 80$, and 90 nm (from top to bottom). Dashed line: chronoamperometric current for $x_0 = 0$ (Cottrell law). Figure 3b–d: peak currents, peak half width, and charge obtained by simulation of case 1 for various x_0 and t_0 . $D = 10^{-9} \text{ m}^2 \text{ s}^{-1}$.

For $x_0 \gg 2\sqrt{Dt_0}$, the charge is independent of x_0 and reaches the value of $0.5642nFAC_0\sqrt{Dt_0}$ (estimated numerically).

When $x_0 \ll 2\sqrt{Dt_0}$, the charge is also independent of x_0 and equal to $2/\sqrt{\pi}nFADC_0\sqrt{Dt}$.

It has to be remembered that derivation of the current is only valid provided that $v \gg 2r_0D/x_0^2$. Any other parameters being unchanged, when x_0 decreases, the rate of diffusion inside TL increases. Consequently, the current density is not homogeneous and the influence of v has to be considered.

Similarly, resolution of eq 6 considering each surface element dA leads to the following expression for the current density:

$$j = \frac{di}{dA} = nFD \left(\frac{\partial C}{\partial x} \right)_{x=0} = nFC_0 \sqrt{\frac{D}{\pi(t-t_1)}} \exp \left(-\frac{x_0^2}{4D(t-t_1)} \right) \quad (11)$$

where t_1 is the time at which the surface element dA is discovered by the bubble. When x_0 is small enough, the exponential term can be neglected and j reaches the Cottrellian expression:

$$j = nFC_0 \sqrt{\frac{D}{\pi(t-t_1)}} \quad (12)$$

j is then independent of x_0 and has exactly the same expression as if the bubble was in contact with the electrode ($x_0 = 0$).²²

3.1.2. Simulations for $t \geq t_0$. When the bubble wall returns after collapse, the solution of Fick's equation cannot be easily found analytically. Therefore, we adopt the explicit finite difference numerical method to simulate the problem.²² The analytical concentration profile found in the previous section (eq 7) was taken as the starting condition. To fit the experimental data, working curves giving the peak current i_p , the peak half width $\Delta t_{1/2}$ and the charge Q for different x_0 and t_0 are generated (cf. Figure 3b–d). Comparison of theory and experiments is described in section 4.

3.2. Case 2: $v \ll 2r_0D/x_0^2$. Here, x_0 is neglected and the current density is given by eq 12. Therefore, the global current

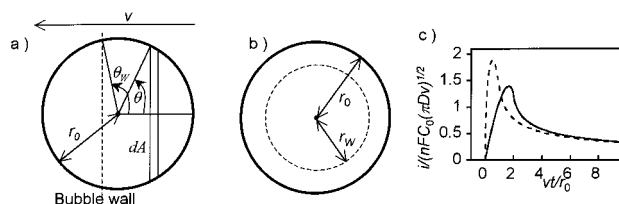


Figure 4. Description of case 2. (a) Case 2a, linear bubble wall (dashed line) and disk electrode of radius r_0 (big solid line). (b) Case 2b, circular bubble wall (dashed line) and disk electrode (big solid line). (c) Nondimensional currents for case 2a (solid line) and case 2b (dashed line).

is obtained by integration of the current density over the electrode area in contact with the solution according to

$$i = \int j \, dA \quad (13)$$

Two geometries are considered. In section 3.2.1, the bubble is supposed to have a radius (R_B) large compared to that of the electrode (r_0) so the bubble wall is approximated by a line (cf. Figure 4a). In order for this condition to be fulfilled, the bubble center must be outside of and remote from the electrode. Since a wide distribution of bubble diameters was previously detected, this assumption is not valid for all the bubbles, but does correspond to at least 20% of them on the basis of the probability measurements reported previously¹³ (taking $R_B > 10r_0$ as an arbitrary criterion for neglecting the curvature of the bubble). Also we suppose that the bubble wall velocity is constant when the bubble meets the electrode, i.e., that $\Delta v/\langle v \rangle$ is small between one side of the electrode and the other (Δv is the difference in the velocity between one side and the other, and $\langle v \rangle$ is the average velocity). This assumption depends on r_0 as well as on the velocity gradient.

Conversely, we suppose in section 3.2.2 that the bubble is circular and centered on the electrode (cf. Figure 4b).

3.2.1. Case 2a: Large Bubble Collapsing with Its Center outside of the Electrode. At time $t = 0$, the wall is at $\theta_w = 0$, and the surface is freed progressively as is shown in Figure 4a. Then $t_{\text{all}} = 2r_0/v$. We suppose that each surface element $dA = 2r_0^2 \sin^2(\theta) \, d\theta$ is brought into contact with the solution at time t_1 ($0 \leq t_1 \leq t_{\text{all}}$). Since the velocity is constant, and the wall linear, t_1 is given by

$$t_1 = \frac{r_0(1 - \cos \theta)}{v} \quad (14)$$

At time t , the wall reaches the angle θ_w ($t = r_0(1 - \cos(\theta_w))/v$). The current density at an angle θ is then

$$j(\theta) = nFC_0 \sqrt{\frac{Dv}{\pi r_0(\cos(\theta) - \cos(\theta_w))}} \quad (15)$$

The total current is obtained by integrating $j(\theta) \, dA$ between 0 and θ_w :

$$i(\theta_w) = nFC_0 r_0^{3/2} \sqrt{\frac{Dv}{\pi}} \psi \quad (16)$$

where

$$\psi = 2 \int_0^{\theta_w} \frac{\sin^2(\theta) \, d\theta}{(\cos(\theta) - \cos(\theta_w))}$$

The form of ψ is given on Figure 4c. The maximum occurs at $t_p = 1.65r_0/v$ and $\psi_p = 4.38$.

For $t_{\text{all}} \leq t$, each surface element contributes to the total current according to

$$i(t) = 2nFC_0 r_0^2 \sqrt{\frac{D}{\pi}} \int_0^\pi \frac{\sin^2(\theta) \, d\theta}{\sqrt{t - \frac{r_0}{v}(1 - \cos(\theta))}} \quad (17)$$

3.2.2. Case 2b: Bubble Collapsing on the Electrode with a Circular Geometry. We suppose now that the bubble is centered on the electrode (cf. Figure 4b), and that at a time t the bubble has a radius r_w . Then, $t = (r_0 - r_w)/v$ and $t_1 = (r_0 - r)/v$ is the time at which the surface element $dA = 2\pi r \, dr$ has been discovered by the bubble. Following the same reasoning as in the previous section, integration of eq 13 leads now to

$$i(t) = nFC_0 \sqrt{\pi D t} \frac{4v(3r_0 - 2vt)}{3} \quad (18)$$

The maximum current occurs for $t_p = r_0/2v$ ($i_p = 4nFC_0 r_0^{3/2} \sqrt{2\pi D v/3}$).

4. Experimental Section Results and Discussion

4.1. Peak Currents Analysis. This section is concerned with the comparison of the sharp current transients observed when chronoamperograms are recorded under 20 kHz ultrasound¹³ with the aim of finding if the experimental behavior can be described by one of the two limiting cases considered above. For a horn to electrode distance of 7 to 10 mm, and an acoustic power of $8.9 \, \text{W cm}^{-2}$, the peak rise time is typically around $1 \, \mu\text{s}$, and the current ca. $3 \, \mu\text{A}$ for a 10 mM concentration of electroactive material. An example of chronoamperogram is given in Figure 1a, for the reduction of $\text{Ru}(\text{NH}_3)_6^{3+}$ in water. In Figure 1b–l, each cavitation spike of Figure 1a is presented at the microsecond time scale.

We first compare the experimental currents to case 2. To get a rise time of around one microsecond, bubble wall velocities of ca. $26 \, \text{m s}^{-1}$ have to be introduced. This leads to currents of ca. $25 \, \mu\text{A}$ for a 10 mM concentration. Case 2b would require only $v = 8 \, \text{m s}^{-1}$, which would give $i_p = 18 \, \mu\text{A}$. Hence, the currents predicted by case 2 are at least six times greater than the experimental ones. Also, the required collapse velocities are small compared to the literature data.^{11,23} Consequently, case 2 is not adapted to describe acoustic bubbles driven at 20 kHz, but may be applicable for slower bubble collapses.

Case 1 was then used to fit all the cavitation spikes shown in Figure 1a. For each experimental peak, a baseline correction (justified in the next section) was applied. Next, we matched the peak height and width with the working curve data. This allows values of x_0 and t_0 to be theoretically deduced. The charge gives less accurate fitting since it results from integration of the whole peak, and then it includes the slight deviation from case 1 sometimes observed in the last part of the peak decay. Comparing the experimental voltammograms to the simulations (cf. Figure 1b–l) gives a very good fit for peaks d, f, h, j, k, and l, whereas peaks b, c, e, g, and i cannot be described by the theory developed in section 3.1. Table 1 gives the values of i_p and $\Delta t_{1/2}$ and, where possible, the deduced values of x_0 and t_0 for all the peaks of Figure 1. The peaks where case 1 is unsuccessful possibly result from a different bubble/electrode distance x_0 before and after the collapse. However, note that x_0 would remain on the same order of magnitude. For example, peak e has a symmetrical shape, resulting from a standard rise

TABLE 1: Peak Currents, Peak Half-Widths, and where Available, Values for x_0 and t_0 for the Cavitation Spikes Described in Figure 1

peak	i_p (μA)	$\Delta t_{1/2}$	x_0 (nm)	t_0 (μs)
b	1.44	3.2		
c	2.00	0.97		
d	2.80	1.72	64 ± 1	0.2 ± 0.01
e	2.29	0.8		
f	2.21	1.17	53 ± 1	0.055 ± 0.01
g	2.16	0.55		
h	2.97	1.67	62 ± 1	0.2 ± 0.02
i	2.75	0.54		
j	3.65	1.24	54 ± 1	0.17 ± 0.01
k	3.20	0.97	46 ± 1	0.07 ± 0.01
l	3.59	2.33	73 ± 2	0.56 ± 0.04

time (ca. 1 μs) which would be compatible with $x_0 \approx 60$ nm, but a decrease of less than 1 μs , compatible rather with $x_0 \approx 30$ nm.

It is not unexpected to observe the variable behavior shown in Table 1 under the conditions used, since the precise behavior of the bubble results from a complex acoustic field (probably influenced by the presence of neighboring bubbles) as well from the local surface roughness. A large range of values is obtained for t_0 (from 0.05 to 0.6 μs), which reveals, even in this apparently periodic signal a partially chaotic behavior. Nevertheless, the experimental t_0 values reveal that most of the time (at least 98% of the acoustic cycle) the bubble covers the electrode, which is a conclusion identical to that shown by Leighton on the basis of simulations performed for high acoustic pressures in solution.²³ Furthermore, x_0 values range between 45 and 75 nm, which implies again small variations of x_0 over the whole chronoamperogram. The presence of a thin layer of solution between the bubble wall and the surface, is thus clearly established and quantified.

From the deduced t_0 values, we can roughly estimate the average bubble wall velocity: t_0 corresponds to the time for the bubble to “discover” or recover the whole electrode, and hence travel through a total distance of $2r_0$ if the bubble is centered on the electrode, or up to $4r_0$ if the bubble is centered outside the electrode. Consequently, t_0 incorporates both the collapse and the expansion velocities, plus eventually a time during which the bubble wall is moving, but outside the electrode surface. Taking the average value of $t_0 = 0.2$ μs , we get an average minimum wall velocity ranging from 160 to 320 m s^{-1} , depending on the bubble position. These high velocities are consistent with Leighton’s simulations of acoustic bubbles oscillating in solution,^{11,23,24} and have to be related also to the high local acoustic pressures estimated in section 4.4. Then, the condition $v \gg 2r_0 D/x_0^2$, necessary for case 1 to be valid, is fulfilled ($2r_0 D/x_0^2 \approx 20$ m s^{-1}). However, it has to be emphasized that the deduced values of t_0 , in contrast those of x_0 , strongly depend on the electrode area introduced in the simulations. Here, we considered that the current density on the electrode is the same everywhere, but if the bubble only partly covers, or only partly discovers the electrode when the collapse and expansion occur, the effective charge electrolyzed is smaller and hence higher t_0 values have to be introduced to compensate these effects. For example, a diminution of 40% of the electrode area leads to t_0 values 2.5 times greater than the ones obtained in Table 1. This may explain the small t_0 values obtained for peaks f and k. The wall velocities nevertheless remain of the order of a few hundred m s^{-1} . Much more information could be obtained if current acquisition and photographic detection were made simultaneously. The photographic detection would lead to the global bubble size evolution,

whereas the electrochemistry measurements would focus on the region of a few tens of nm between the surface and the bubble, impossible to reach with optical detection. A more complete model, incorporating the wall velocity could then be developed.

4.2. Origin of the Baseline Current. In Figure 1a, the baseline current (i.e., for $t \leq 0$), although small (0.1 μA) is not zero. Often, this baseline is also curved and, for example, a slope of ca. 0.004 $\mu\text{A } \mu\text{s}^{-1}$ is obtained before peak b. Since the bubble covers the electrode, a nonzero current reveals that some solution is penetrating between the electrode and the bubble wall. This arises from shape deformation and/or bubble movement away from the surface, which can be characterized via the average velocity u of the bubble perpendicularly to the surface: $u = dx_0/dt$. If u is small enough compared to the rate of diffusion inside TL ($u \ll D/x_0$), the current is steady state and only proportional to the charge (and then the volume of solution) penetrating above the electrode per unit of time:

$$i = \frac{dq}{dt} = nFAC_0u \quad (19)$$

Note that any charge penetrating inside TL is immediately electrolyzed, so both the concentration and the concentration gradient in the thin layer are then still close to zero for $t \leq 0$. Then, when the bubble collapses (at $t \geq 0$), diffusion of the electroactive material is unaffected by the slow bubble movement for $t \leq 0$. The global current is therefore only the sum of the base-line current and the current due to the bubble implosion.

A slope in the current may indicate that u is not constant, allowing us to speculate on the average acceleration a of the bubble wall:

$$a = \frac{du}{dt} = \frac{1}{nFAC_0} \left(\frac{di}{dt} \right) \quad (20)$$

For Figure 1, this analysis gives $u \approx 1.2 \times 10^{-4}$ m s^{-1} , and $a = 5.2$ m s^{-2} for the base line of peak b. Note that $u \ll D/x_0$ is here entirely fulfilled, which validates our approach. Then, in one acoustic cycle, the bubble moves approximately 7 nm away from its previous position when there is no acceleration and at most 20 nm for peak b, which is again consistent with the variations of x_0 observed in section 4.1. Since u is slow compared to the collapse velocity v , there is no need to include it in the description of the collapse behavior, apart from subtracting the baseline, which justifies the procedure done in the previous section.

Returning to the simulations made in the previous section, we can now speculate on an explanation for the slight difference sometimes observed between the simulations and the experiment at the beginning of the peak (i.e., peaks f, j, k, and l), where the increase of the experimental peak current starts relatively slowly, compared to the simulations. This extra current possibly results from an accelerated movement of the bubble before or at the beginning of the collapse, until favorable conditions are fulfilled for a fast and total collapse. Moreover, the deviations from the model in the decrease of the peak current (i.e., peak h) can also be attributed to an additional current provoked by a complex bubble behavior. The behavior of an acoustic bubble close to a surface is now explained for an entire acoustic cycle.

4.3. Limitations of the Model. **4.3.1. Influence of the Electrode to Horn Distance.** We report next chronoamperometry experiments similar to those described in Figure 1a, but performed at a 2 mm horn to electrode distance with the same ultrasound power (8.9 W cm^{-2}). The chronoamperograms are shown in Figure 5. A dramatic change in the signal shape can

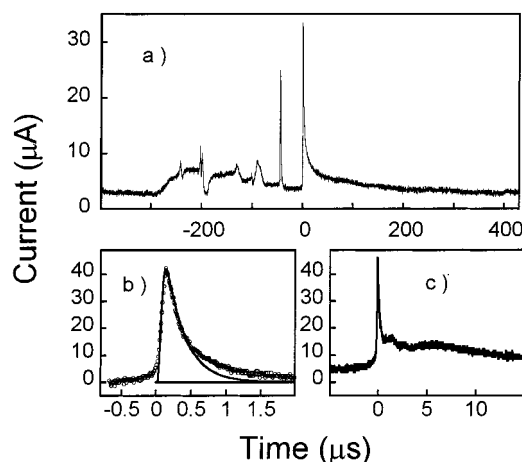


Figure 5. Chronoamperometric currents recorded for different cavitating bubbles obtained with a 50 mM $\text{K}_3\text{Fe}(\text{CN})_6$ water solution under sonication at 20 kHz with a 13 mm flat horn. Electrode to horn distance: 2 mm. Electrode diameter: 32 μm . Acoustic power: 8.9 W cm^{-2} . Electrode potential: -0.8 V vs Pt . (b) Experimental spike (circles) and simulated spike (solid line) with $x_0 = 26 \text{ nm}$ and $t_0 = 0.05 \mu\text{s}$. (c) Rebound in the cavitation spike.

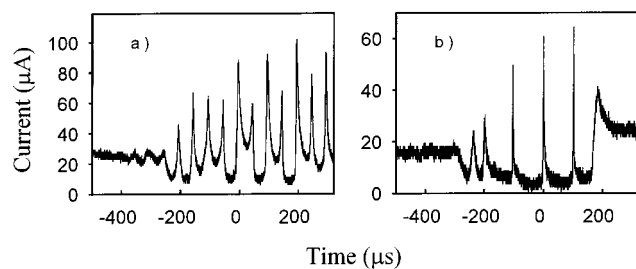


Figure 6. Chronoamperometric currents recorded for different cavitating bubbles obtained with a 50 mM $\text{K}_3\text{Fe}(\text{CN})_6$ water solution under sonication at 20 kHz with a 13 mm flat horn. Electrode diameter: 139 μm . Acoustic power: 8.9 W cm^{-2} . Electrode potential: -0.8 V vs Pt . Electrode to horn distances: (a) 7 mm and (b) 2 mm.

be observed: the periodic behavior becomes less frequent (cf. Figure 5a), and when observed lasts at most five acoustic cycles, which reveals a transition between stable and transient cavitation, a well described phenomenon.¹¹ The maximum peak current is increased by a factor of more than two and the rise time of the peaks decreases to around 200 ns. Also, the global shape of the peak deviates from the typical ones produced by the simulations, often showing a longer second peak superimposed on the first one, as observed in Figure 5c). This may speculatively be attributed to a bubble rebound after a violent collapse, a phenomenon already observed in solution and for laser generated bubbles.⁶ The decrease time is then longer than expected from the simulations because the bubble movement is more complex. Nevertheless the simulation of a peak without rebound gives excellent agreement with the simulation (cf. Figure 5b). To explain the very small rise time of this peak, $x_0 = 26 \pm 2 \text{ nm}$ and $t_0 = 0.05 \pm 0.01 \mu\text{s}$ need to be introduced.

Note that increasing the acoustic power up to 40 W cm^{-2} and performing the same experiment did not affect the chronoamperometric peak characteristics quantitatively whatever the horn to electrode distance, probably because shielding of the acoustic field by an increased number of bubbles occurs, thus leaving the local acoustic pressure largely unchanged.

4.3.2. Influence of the Electrode Size. Figure 6 shows two chronoamperograms obtained for a 139 μm diameter electrode. This signal presents the same periodic trends as one obtained at the 32 μm electrode, but the peaks have higher rise times

and widths. Normalized to an equivalent concentration, the peak current is only 6 times greater (instead of 18 times if the current was proportional to the electrode area as assumed in our model). However, the axial velocity u deduced from the baseline current remains nearly the same ($u = 1.3 \times 10^{-4} \text{ m s}^{-1}$).

Noting that case 1 is applicable only if $v \gg 2r_0D/x_0^2$ and taking $x_0 = 50 \text{ nm}$ now leads to $v \gg 56 \text{ m s}^{-1}$. This requirement has to be fulfilled over the whole surface area and throughout the collapse and expansion phases, and is then probably not respected. Furthermore, v is possibly slower for large bubbles, at least at the beginning of the collapse.^{23,24} To simulate those peaks, the bubble dynamics need to be incorporated in the model, which is beyond the scope of the present study. Nevertheless, a decrease of the electrode to horn distance leads us to observe thinner peaks, which is consistent with a decrease of both x_0 and t_0 , and then an increase of v (cf. Figure 6b).

4.4. Origin of the Thin Layer. For bubble dynamics in solution, the fluid viscosity is usually neglected. Blake's simulations of bubble/surface interaction also neglect the viscosity.^{2,25,26} The reason for that is that the viscous damping term is proportional to $1/R_B$ in homogeneous solution, and thus can be neglected for large spherical bubbles.¹¹ However, in the cases explored in this paper, the bubble covers the surface over a large area and so the net force caused by the viscosity shear stress on the surface is probably important. In fact, the viscosity of the solution imposes that the fluid velocity on the surface is zero. Consequently, the collapse cannot occur if the bubble touches the electrode ($x_0 = 0$) and a thin layer of solution between the bubble and the surface has to be introduced.

Usually, it is assumed that when the external pressure becomes higher than the internal one, collapse occurs. In our situation, it seems that the viscosity term has to be introduced in the pressure balance.^{5,11} The condition for collapse is then

$$P_A + P_H + \frac{2\tau}{R_B} > P_V + P_G + \sigma \quad (21)$$

where P_A , P_H , τ , P_V , P_G , and σ are respectively the acoustic pressure, the hydrostatic pressure, the surface tension, the vapor pressure of the solvent, the gas pressure in the bubble, and the shear viscosity term. For large bubbles, the surface tension can be neglected.¹¹ Considering that σ is much greater than P_V and P_G , and neglecting the hydrostatic pressure as well leads to

$$P_A > \sigma \quad (22)$$

For a thin layer, σ is on the order of $\eta v/x_0$, where η is the shear viscosity, and thus increases when x_0 decreases. This explains why collapse does not occur for $x_0 = 0$. Our suggestion is that the bubble moves slightly away from the surface in order for inequality 22 to be fulfilled. When the local conditions are favorable, a very fast and violent collapse occurs. Knowing x_0 allows one to deduce an approximate local acoustic pressure. Taking $v = 200 \text{ m s}^{-1}$ and $x_0 = 60 \text{ nm}$ for Figure 1a leads to $P_A \approx 30 \text{ bar}$, whereas $P_A \approx 250 \text{ bar}$ would be obtained for Figure 5b. The acoustic pressure drop is therefore very important when the horn to electrode distance decreases.

P_A is then much higher than the average acoustic pressure that can be deduced via calorimetric measurements.^{5,11,27} On the other hand, the bubble shape is supposed to be very different from the spherical one. All these experimental results show that the local conditions are far remote from the ones previously introduced in the simulations, and may also explain why no microjet is observed. The microjet may simply just not have time to develop under the pertaining conditions.

The examples described in this paper reveal that electrochemical measurements are powerful tools to measure local pressures.

5. Conclusion

We have demonstrated that electrochemical measurements can give unique information about interfacial cavitation, at the nanosecond and nanometer scales otherwise impossible to attain with other techniques, such as photographic detection. All the experimental observations are consistent with a very fast bubble collapse at a distance of few tens of nanometers above the surface. The distance between the bubble and the surface varies slightly during one acoustic cycle. When the local acoustic pressure is increased, the behavior becomes more chaotic, but same trends are observed. The resulting diffusion layer and collapse times are nevertheless smaller. Consequently, by allowing a direct quantification of the cavitation at a surface, this paper opens up the possibility for new interpretations of ultrasound effects at surfaces.

Acknowledgment. We gratefully thank EPSRC for financial support.

References and Notes

- (1) Crum, L. A., Ed. *Sonochemistry and Sonoluminescence*; Kluwer Academic Publishers: London, 1999; Vol. 524.
- (2) Blake, J. R., Ed. *Acoustic Cavitation and Sonoluminescence*; Kluwer Academic Publishers: London, 1999; Vol. 357, p 201.
- (3) Didenko, Y. T.; McNamara, W. B.; Suslick, K. S. *J. Am. Chem. Soc.* **1999**, *121*, 5817.
- (4) Mason, T. J. *Philos. Trans. R. Soc. London Ser. A: Math. Phys. Eng. Sci.* **1999**, *357*, 355.
- (5) Mason, T. J. *Chem. Br.* **1986**, *22*, 661.
- (6) Philipp, A.; Lauterborn, W. *J. Fluid Mech.* **1998**, *361*, 75.
- (7) Rosenberg, L. D. *Ultrasonic News Winter* **1960**, 16.
- (8) Compton, R. G.; Eklund, J. C.; Marken, F. *Electroanalysis* **1997**, *9*, 509.
- (9) Crum, L. A. *J. Phys.* **1979**, *11*, C8.
- (10) Hill, C. R. *Physical Principles of Medical Ultrasonics*; Ellis Horwood, 1986.
- (11) Leighton, T. G. *The Acoustic Bubble*; Academic Press: New York, 1994.
- (12) Plesset, M. S.; Chapman, R. B. *J. Fluid Mech.* **1971**, *47*, 283.
- (13) Maisonhaute, E.; White, P. C.; Compton, R. G. *J. Phys. Chem. B* **2001**, *105*, 12087.
- (14) Amatore, C.; Maisonhaute, E.; Simonneau, G. *Electrochem. Commun.* **2000**, *2*, 81.
- (15) Amatore, C.; Maisonhaute, E.; Simonneau, G. *J. Electroanal. Chem.* **2000**, *486*, 141.
- (16) Birkin, P. R.; Delaplace, C. L.; Bowen, C. R. *J. Phys. Chem. B* **1998**, *102*, 10885.
- (17) Birkin, P. R.; SilvaMartinez, S. J. *Electroanal. Chem.* **1996**, *416*, 127.
- (18) Birkin, P. R.; SilvaMartinez, S. *Anal. Chem.* **1997**, *69*, 2055.
- (19) Wightman, R. M.; Wipf, D. O. *Electroanal. Chem.* **1989**, *15*, 267.
- (20) Margulis, M. A.; Maltsev, A. N. *Russ. J. Phys. Chem.* **1969**, *43*, 592.
- (21) Marken, F.; Akkermans, R. P.; Compton, R. G. *J. Electroanal. Chem.* **1996**, *415*, 55.
- (22) Bard, A. J.; Faulkner, L. R. *Electrochemical Methods*; Wiley: New York, 1980.
- (23) Leighton, T. G. *Ultrasonics* **1989**, *27*, 50.
- (24) Leighton, T. G.; Walton, A. J.; Field, J. E. *Ultrasonics* **1989**, *27*, 370.
- (25) Blake, J. R.; Hooton, M. C.; Robinson, P. B.; Tong, R. P. *Philos. Trans. R. Soc. London Ser. A: Math. Phys. Eng. Sci.* **1997**, *355*, 537.
- (26) Blake, J. R.; Keen, G. S.; Tong, R. P.; Wilson, M. *Philos. Trans. R. Soc. London Ser. A: Math. Phys. Eng. Sci.* **1999**, *357*, 251.
- (27) Lorimer, J. P.; Mason, T. J. *Chem. Soc. Rev.* **1987**, *16*, 239.